

# Microchannel Cooling Performance Evaluation of Al<sub>2</sub>O<sub>3</sub>, SiO<sub>2</sub> and CuO Nanofluids Using CFD

Roy Strandberg, Dustin Ray and Debendra Das\*

Department of Mechanical Engineering, University of Alaska Fairbanks, P.O. Box 755905, Fairbanks, AK, 99775-5905, USA.

## Abstract

In this study, the performance of a microchannel heat sink (MCHS) filled with various nanofluids and the corresponding base fluid without nanoparticles are examined using a three-dimensional conjugate heat transfer and fluid dynamic finite-volume model over a range of conditions. The model incorporates a fixed heat flux of 1,000,000 W/m<sup>2</sup> at the base of the solid domain. The thermophysical properties of the fluids are based on empirically obtained correlations, and vary with temperature. Nanofluids considered include 60% Ethylene Glycol/40% Water solutions with CuO, SiO<sub>2</sub>, and Al<sub>2</sub>O<sub>3</sub> nanoparticles dispersed in volumetric concentrations ranging from 1 to 3%. The flow conditions analyzed are in the laminar range (50 ≤ Re ≤ 300), and consider multiple inlet temperatures. The analyses predict that when compared on an equal Reynolds number basis, the 60% EG/3% CuO nanofluid exhibits the highest heat transfer coefficient, and the largest reduction in average base temperature. At an inlet Reynolds number of 300, and an inlet temperature of 308K the nanofluid is predicted to have an average heat transfer coefficient that is 30% higher than that of the base fluid, while the average temperature on the base of the heat exchanger is 1K lower than that of the base fluid. In contrast, the inlet pressure required for these entering conditions is 192% higher than that for the base fluid, while the required hydraulic power to drive the flow is 366% higher than that of the base fluid.

**Keywords:** *Microchannel cooling, Nanofluids, CuO, SiO<sub>2</sub>, Al<sub>2</sub>O<sub>3</sub>, CFD.*

## Nomenclature

$A$	Heat transfer surface area	$\dot{V}$	Volumetric flow
$c_p$	Specific heat	$R$	Thermal resistance
$f$	Fanning friction factor	$Re$	Reynolds number
$g$	Gravitational acceleration	$\dot{W}$	Hydraulic power
$h$	Convective heat transfer coefficient	$T$	Temperature
$H$	Fin height	<b>Greek symbols</b>	
$k$	Thermal conductivity	$\alpha$	Channel aspect ratio
$L$	Length	$\beta_1$	Channel aspect ratio
$\dot{m}$	Mass flow rate	$\mu$	Dynamic viscosity
Nu	Nusselt number	$\eta$	Fin efficiency
$\Delta p$	Pressure drop	$\phi$	Volumetric concentration
$q$	Total heat transfer rate	$\rho$	Density
$q''$	Heat flux	<b>Subscripts</b>	
$V$	Liquid velocity	$i$	Inside

\* Corresponding author

<i>cap</i>	Capacitive	<i>nf</i>	Nanofluid
<i>con</i>	MCHS base	<i>s</i>	Solid nanoparticle
<i>f</i>	Base fluid	<i>th</i>	Heat sink thermal resistance
<i>fin</i>	Fin	<i>w</i>	MCHS wall

## 1. Introduction

Nanofluids are colloidal heat transfer fluids that are comprised of a conventional “base fluid,” such as glycol, water or oil, that contain nanoparticles in a stable suspension. The nanoparticles typically have a characteristic dimension on the order of a 100nm. These fluids have been shown to exhibit significantly enhanced thermal conductivity compared to conventional fluids. In some cases, the enhancement in thermal conductivity significantly exceeds that predicted by previously developed correlations for liquids with suspended solids [1, 2]. In recent years there has been a great deal of research devoted to characterizing nanofluids’ transport properties, and determining if their characteristics can be exploited to improve the performance of heat transfer processes. Chon et al. [3] conducted an experimental study of thermal conductivity of nanofluids comprised of deionized water with alumina nanoparticles in sizes ranging from 11 nm to 150 nm. This work appears to validate the theoretical model proposed by Jang and Choi [4] for nanofluids of this type. Chon et al. also concluded that nanofluids’ thermal conductivity increases with temperature, and decreasing particle size. More recently, a series of published studies have yielded a fairly comprehensive set of transport property data for nanofluids with comprised of  $\text{Al}_2\text{O}_3$  and CuO dispersed in 60% ethylene glycol (EG). Vajjha and Das [5] conducted experimental work that yielded correlations based on the form developed by Koo and Kleinstreuer [6] for the thermal conductivity of CuO/60% EG and  $\text{Al}_2\text{O}_3$ /60% EG nanofluids over relatively broad ranges temperature and volumetric concentrations. Other detailed correlations for viscosity and specific heat have been developed by Namburu et al. [7] and Vajjha and Das [8], respectively.

Microchannel heat sinks (MCHS) are devices employing fluids flowing through extremely small channels alternating with fins to facilitate heat transfer. These devices have been developed to support the operation of electronics and other applications where there is a need for high-density heat rejection. In a case where a heat-generating device (such as an integrated circuit) is placed in direct contact with the MCHS, heat is conducted through the base into the fins, while the fluid flowing through the channels extract the heat primarily via convection, usually in the laminar regime. Figure 1 illustrates the configuration considered for this study. MCHS, due to their geometry, have relatively large heat transfer surface area relative to heat sinks of equal volume but with larger channels. Nanofluids have been investigated in previous experimental studies and numerical analyses in regard to their potential use in microchannel heat sinks. Faulkner et al. [9] conducted an experimental study using water base nanofluids demonstrating the potential for performance benefits of nanofluids relative to conventional heat transfer fluids when used in a heat sink with extremely small flow channels. The nanofluids tested included  $\text{Al}_2\text{O}_3$  nanoparticle and other nanoparticles dispersed in water. Their experiments were conducted using heat sinks with channels 0.5 mm wide and 6 mm deep. These dimensions are larger than those loosely defined as falling into the microchannel category, however the results of the study still offer insights into the flow and heat transfer characteristics of microchannel heat sinks. Their study demonstrated that these meso-channel heat sink devices with nanofluids successfully achieved high rates of heat extraction under laminar flow conditions. Ho, et al. [10] performed an experimental study testing the thermal performance of a copper MCHS with  $\text{Al}_2\text{O}_3$ /water nanofluid against that of water for  $226 < \text{Re} < 1,676$ . The authors measured a substantial increase in the inside heat transfer coefficient

for the nanofluids relative to that for water over the range of Reynolds numbers tested. Lee and Mudawar [11], Peng, et al. [12] and Jung, et al. [13] also performed experimental studies with nanofluids in MCHS and found that the nanofluid filled MCHS tested offered higher rates of heat rejection than the MCHS filled with the base fluid.

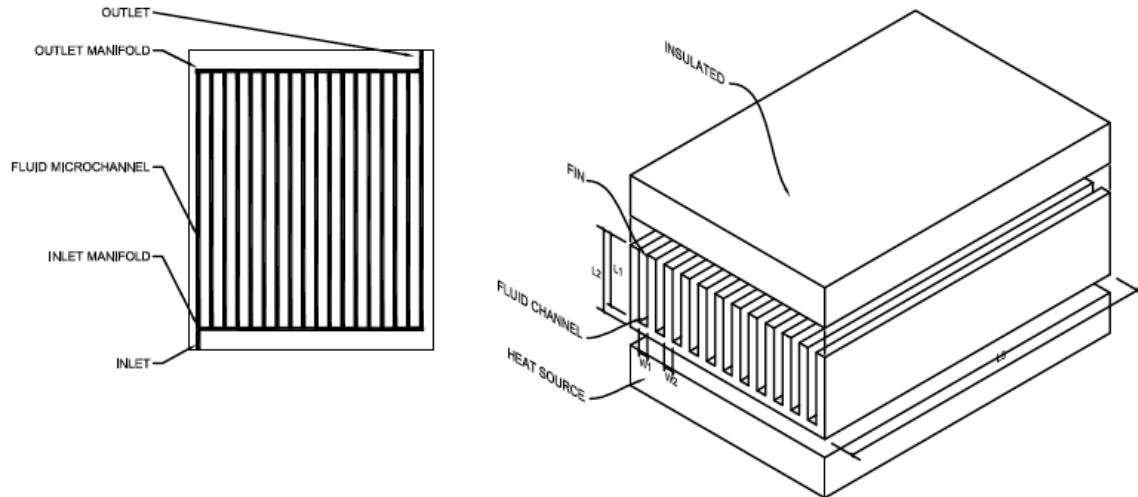


Figure 1. Microchannel heat sink configuration.

Chein and Huang [14] conducted a computational study using theoretical and empirically determined transport property correlations for nanofluids to analyze the performance of a MCHS with a Cu/water nanofluid in various concentrations. Koo and Kleinstreuer [15] also conducted an analysis of MCHS performance with nanofluids using a variety of theoretical models for the heat transfer and rheological properties. They developed a numerical model for heat transfer in rectangular microchannels 100  $\mu\text{m}$  wide and 300  $\mu\text{m}$  deep with steady, laminar flow and constant heat flux. The investigators concluded that microchannel heat sinks may offer better heat transfer performance with nanofluids (compared to those with conventional heat transfer fluids). Jang and Choi [16] conducted another computational study of MCHS performance using theoretical models of nanofluid transport properties. Their analysis predicted a 10% improvement in the heat rejected by the nanofluid filled heat sink as compared to the heat sink with a conventional fluid, when pumping energy was held constant. Leela [17] conducted a numerical study of MCHS filled with  $\text{Al}_2\text{O}_3$ /water nanofluid in various concentrations and considering various nanoparticle diameters over a range of Reynolds numbers. The study showed that the nanofluid enhanced heat transfer relative to the base fluid. Snoussi et al. [20] have presented results of laminar flow computations using the CFD code Fluent in a microchannel heat sink using water-based aluminum oxide and copper nanofluids. Their results show an increase in heat transfer performance of 14-20% by the nanofluids over pure water.

During the past two decades, due to steady advancements in military and civilian airborne and space-based electronics and associated increases in the density thereof, the need for more effective thermal management has increased in parallel. These challenges can be met by developing compact microchannel heat sinks and cold plates. The encyclopedia by Bar-Cohen [18] is a good source to obtain the governing equations, thermal and fluid dynamic analyses and the optimization techniques for designing such cooling equipment. In order to cope with the high-density heat fluxes generated in such new devices, researchers are also exploring more efficient coolants such as

nanofluids. Two-phase heat transfer and flow in microchannels and critical heat flux phenomena with nanofluids in cooling systems in electronics are described in detail by Thome [19].

The purpose of this study is to examine the performance of a microchannel heat sink with nanofluids and the associated base fluid using a finite volume computational model. The performance of MCHS with 60% (by mass) ethylene glycol/water solution (the base fluid) and several different nanofluids in various concentrations will be compared. The freezing point of the base fluid is  $-48.3^{\circ}\text{C}$  [21], which makes the fluid suitable for certain aeronautical and space applications. The nanoparticles considered include copper oxide (CuO), aluminum oxide ( $\text{Al}_2\text{O}_3$ ) and silicon dioxide ( $\text{SiO}_2$ ), in volumetric concentrations ranging up to 3%. The model developed for the analysis is a three-dimensional domain comprised of solid and liquid domains. The solid domain represents the fin and the liquid domain represents the heat transfer fluid flowing through the heat exchanger. The liquid and solid domains are mathematically coupled at the boundary to allow for the exchange of data during the simulation thereby facilitating solution generation for both the heat transfer and fluid dynamic problems posed. With the exception of the Chein and Huang's [14] study mentioned earlier, all of the computational studies [15-17] depend upon theoretical models for nanofluid transport properties. In the current study, transport properties for the nanofluids examined are based on empirical data. Furthermore, the temperature dependencies of the fluids' transport properties are incorporated into the model. For this reason, this analysis offers the potential for better MCHS modeling results than those in other studies. Furthermore, the current study examines the performance of a wider array of nanoparticles and concentrations than in other studies already documented.

## 2. Theory

In this analysis, the performance of MCHS is analyzed with heat transfer fluids of several different compositions. These include 60% ethylene glycol/40% water solution (heretofore referred to as 60% EG) and three types of nanofluids comprised of a 60% EG base fluid with CuO,  $\text{Al}_2\text{O}_3$ , or  $\text{SiO}_2$  nanoparticles, uniformly dispersed in volumetric concentrations of 1%, 2% and 3%. Thermophysical property data for the 60% EG were taken from ASHRAE Fundamentals [21].

For all curve – fits applied to 60% EG property data (Eqs. 1, 3, 6 and 8 below),  $R^2 > 0.99$ . These correlations are applicable for 60% EG between  $273\text{K} < T < 370\text{K}$ .

### 2.1 Density

For density of the 60% EG, a polynomial curve fit was applied to the ASHRAE data. The equation for the fitted curve is

$$\left(\frac{\rho}{\rho_o}\right)_{bf} = A + B\left(\frac{T}{T_o}\right) + C\left(\frac{T}{T_o}\right)^2 \quad (1)$$

where  $\rho_o = 1091.66 \text{ kg/m}^3$ ,  $T_o = 273.15\text{K}$ ,  $A = 0.9247$ ,  $B = 0.2414$ , and  $C = -0.1661$ .  $R^2 = 1$ , and the curve-fit error is 0.01%. Pak and Cho [1] first adopted a relationship for the effective density of nanofluids based on earlier work on fluid/microparticle mixtures. Their correlation is used to compute the density of the nanofluid in the following analyses. It is stated as

$$\rho_{nf} = \phi\rho_s + (1 - \phi)\rho_{bf} \quad (2)$$

where the *nf*, *s*, and *bf* subscripts mean nanofluid, solid nanoparticle, and base fluid, respectively.

## 2.2 Specific Heat

For specific heat of the 60% EG, the following curve fit was applied to the ASHRAE data. The equation for the fitted curve is

$$\left(\frac{c_p}{c_{p,o}}\right) = A + B \left(\frac{T}{T_o}\right) \quad (3)$$

where  $c_{p,o}=3042.02$  J/kg•K,  $A=0.6185$  and  $B=-0.3814$ .  $R^2=1$ , and the curve fit error is 0.01%. Buongiorno [22] developed a relation for effective specific heat of nanofluids. Buongiorno's correlation is employed for evaluating the specific heat of CuO and SiO<sub>2</sub> nanofluids. It is stated as

$$c_{p,nf} = \frac{\phi \rho_s c_{p,s} + (1-\phi) \rho_{bf} c_{p,bf}}{\rho_{nf}} \quad (4)$$

From experiments on Al<sub>2</sub>O<sub>3</sub> nanoparticles in 60% EG, Vajjha and Das [8 or 23] developed a specific heat correlation. It is stated as

$$\frac{c_{p,nf}}{c_{p,bf}} = \frac{\left(\left(\frac{A T}{T_o}\right) + B \left(\frac{c_{p,s}}{c_{p,bf}}\right)\right)}{(C + \phi)} \quad (5)$$

where  $A = 0.24327$ ,  $B=0.5179$  and  $C=0.4250$  (these are all dimensionless parameters) and  $315$  K <  $T < 363$  K;  $0.01 < \phi < 0.1$ . Also,  $c_p$  is in kJ/(kg.K).

## 2.3 Viscosity

For viscosity of water (in Pa•s), a correlation presented in White [24] was selected. The equation is stated as:

$$\ln\left(\frac{\mu}{\mu_o}\right)_w = A + B \left(\frac{T_o}{T}\right) + C \left(\frac{T_o}{T}\right)^2 \quad (6)$$

where  $T_o=273.15$  K and  $\mu_o=0.001792$  Pa•s,  $A=-1.94$   $B=-4.80$  and  $C=6.74$ , with accuracy of  $\pm 1\%$ . For viscosity of the 60% EG (in Pa•s), a similar equation was used. This correlation was reported in Ray [25] and was developed from data presented in [21]. For this liquid,  $\mu_o = 0.01179 \frac{kg}{m \cdot s}$ ,  $A=-4.976$ ,  $B=-1.942$  and  $C=6.9088$ .  $R^2=1$ , and the curve-fit error is 0.01%.

Vajjha and Das [23] presented the following correlations based on previous experiments for computing the viscosity (in mPa.s) of nanofluids comprised of CuO, Al<sub>2</sub>O<sub>3</sub> and SiO<sub>2</sub> nanoparticles dispersed in 60% EG base fluid

$$\frac{\mu_{nf}}{\mu_{bf}} = A e^{-B \cdot \phi} \quad (7)$$

$A = 0.9830$  and  $B = 12.9590$  for Al<sub>2</sub>O<sub>3</sub> ( $d_p=45nm$ ) with  $\phi$  up to 10% ( $0 < \phi < 0.10$ )

$A = 0.9197$  and  $B = 22.8539$  for CuO ( $d_p=29nm$ ) with  $\phi$  up to 6% ( $0 < \phi < 0.06$ )

$A = 1.092$  and  $B = 5.954$  for SiO<sub>2</sub> ( $d_p=20nm$ ) with  $\phi$  up to 10% ( $0 < \phi < 0.10$ )

This viscosity correlation was developed for  $273K < T < 360K$ . The maximum deviation of the fitted curves from experimental data was 8%.

## 2.4 Thermal Conductivity

For thermal conductivity of the 60% EG, a polynomial curve fit was applied to the ASHRAE data. The equation of this curve fit is

$$\left(\frac{k}{k_o}\right)_{bf} = A + B \left(\frac{T}{T_o}\right) + C \left(\frac{T}{T_o}\right)^2 \quad (8)$$

where  $k_0=0.342$  W/m.K,  $A=-0.2939$   $B=1.981$  and  $C=-0.6868$ .  $R^2=0.999$ , and the curve fit error is 0.11%.

From experiments on CuO and Al<sub>2</sub>O<sub>3</sub> nanoparticles dispersed in 60% EG, Vajjha and Das [5] developed a thermal conductivity correlation based on an improvement of the Koo-Kleinstreuer [6] model.

$$k_{nf} = \left( \frac{k_s + 2k_{bf} - 2\phi(k_{bf} - k_s)}{k_s + 2k_{bf} + \phi(k_{bf} - k_s)} \right) k_{bf} + 5 \times 10^4 \beta \phi \rho_{bf} c_{p,bf} \sqrt{\frac{\kappa T}{\rho_s d_p}} f(T, \phi) \quad (9a)$$

where  $f(T, \phi) = (2.8217 \times 10^{-2} \phi + 3.917 \times 10^{-3}) \frac{T}{T_0} - (3.0669 \times 10^{-2} \phi + 3.91123 \times 10^{-3})$ .

For nanofluids comprised of Al<sub>2</sub>O<sub>3</sub> nanoparticles,

$$\beta = 8.4407(100\phi)^{-1.07304} \quad (9b)$$

while for nanofluids comprised of CuO nanoparticles,

$$\beta = 9.881(100\phi)^{-0.9446} \quad (9c)$$

for nanofluids comprised of SiO<sub>2</sub> nanoparticles [26],

$$\beta = 1.9526(100\phi)^{-1.4594} \quad (9d)$$

These correlations apply for 293K < T < 363K. For Al<sub>2</sub>O<sub>3</sub> 0.01 <  $\phi$  < 0.10, while for CuO 0.01 <  $\phi$  < 0.06. For SiO<sub>2</sub> 0.01 <  $\phi$  < 0.10. The average deviation of the correlation from experimental data is 0.23%, 5.74% and 1.16% respectively.

The first term of the Eq. (9a) is the well-known Hamilton-Crosser [27] equation for computing the thermal conductivity of a two-phase substance (solid particles in a liquid matrix). The second term of the same equation was developed to take into account the Brownian motion associated with the nanoparticles that enhances the thermal conductivity of the fluid.

For this analysis, all of the thermophysical properties are evaluated for Al<sub>2</sub>O<sub>3</sub> nanoparticles with a diameter of 45 nm; CuO nanoparticles have a mean diameter of 29 nm; and SiO<sub>2</sub> nanoparticles have a mean diameter 20 nm.

## 2.5 Fluid Flow Parameters

The Reynolds number of the liquid flow through of the microchannel is computed using the equation

$$Re = \frac{\rho V D_h}{\mu} \quad (10)$$

The Nusselt number for single phase flows in a rectangular microchannel depends on geometry and the boundary condition. This dimensionless parameter represents the ratio of convective to conductive heat transfer across a boundary. From Kandalikar et al. [28], for a constant temperature boundary condition the average Nusselt number is calculated using the following correlation.  $Nu_T = 7.541(1 - 2.610\alpha_c + 4.970\alpha_c^2 - 5.119\alpha_c^3 + 2.702\alpha_c^4 - 0.548\alpha_c^5)$  (11a) where  $\alpha_c$  is aspect ratio. For a constant circumferential wall temperature, and uniform axial heat flux, boundary condition the Nusselt number is

$$Nu_{H1} = 8.235(1 - 2.0421\alpha_c + 3.0853\alpha_c^2 - 2.4765\alpha_c^3 + 1.0578\alpha_c^4 - 0.1861\alpha_c^5) \quad (11b)$$

For a constant circumferential and axial heat flux, the Nusselt number correlation is

$$Nu_{H1} = 8.235(1 - 10.6044\alpha_c + 61.1755\alpha_c^2 - 155.1803\alpha_c^3 + 176.9203\alpha_c^4 - 72.9236\alpha_c^5) \quad (11c)$$

The parameter  $\alpha_c$  is the aspect ratio of the microchannel (width to height).

These correlations share one key feature. That is, the Nusselt number is dependent solely upon geometry, versus Reynolds and Prandtl number as in correlations applicable to flows in the turbulent regime. This represents a divergence from dimensionally similar flows at larger scales,

where Nusselt number under fully developed, laminar flows are not dependent upon aspect ratio. Quite often, the Nusselt number under laminar flow regimes is constant. Due to the flow configurations and viscosity of the fluids, it is expected that the Reynolds number will typically remain in the laminar range. These correlations are based on studies of single-phase liquids; studies of nanofluids have focused on the theoretical possibility that the suspended nanoparticles boost convective heat transfer through mechanisms unique to nanofluids. These effects may include effects such as thermophoresis or thermal dispersion, and are theorized to increase the effectiveness of convective heat transfer (the increase in thermal conductivity notwithstanding). For simplicity, we use the single-phase relation for this study.

Note that due to the small physical dimensions of a MCHS, entrance effects may not necessarily be neglected without further consideration. Previous research by Han [29] has shown that the hydrodynamic and thermal entrance length for a MCHS may be computed using the relations:

$$L_h = 0.026D_h Re \quad (12)$$

Previous researchers have collected data on the Nusselt numbers in the thermal developing region for MCHS with rectangular channels of various aspect ratios with conventional fluids. These data are characterized by very short region where the Nusselt number steeply drops to within approximately 10% of the fully developed value (over approximately 2.5% of the theoretical thermal entrance zone length), and then steadily drops to the fully developed value. This Nusselt number profile in the entrance region is typical for the  $\alpha_c$  studied here. Depending on a variety of factors, the thermal entrance region may exceed the length of the MCHS. In these cases, the average Nusselt number considering the entrance region thermal profile is higher than the fully developed value. From [28], the following polynomials were applied to generate Nusselt number curves for purposes of comparison:

$$Nu_{fd,3} = \frac{8.2321+1.2771\alpha_c+2.2389\alpha_c^2}{1+2.0263\alpha_c+0.29805\alpha_c^2+0.0065322\alpha_c^3} \quad (13a)$$

$$Nu_{fd,4} = \frac{8.2313-2.295\alpha_c+7.928\alpha_c^2}{1+1.9349\alpha_c+0.92381\alpha_c^2+0.0033937\alpha_c^3} \quad (13b)$$

$$Nu_{z,4} = \frac{36.738+17559z^++555480(z^+)^2}{1+2254z^++66172(z^+)^2+1212.6(z^+)^3}, \text{ for } \alpha_c = 0.1 \quad (13c)$$

$$Nu_{z,4} = \frac{30.354+13842z^++783440(z^+)^2}{1+1875.4z^++154970(z^+)^2-8015.1(z^+)^3}, \text{ for } \alpha_c = 0.25 \quad (13d)$$

when computing  $Nu$ , the non-dimensional axial coordinate is defined by the following equation.

$$z^+ = \frac{z}{RePr} \quad (14)$$

where,  $z^+$  is the axial coordinate in the domain, and the Reynolds number and Prandtl number are computing at the inlet of the domain.

For this study,  $\alpha_c=0.143$ . In order to calculate  $Nu_{z,3}$  for this  $\alpha_c$  interpolation between  $\alpha_c=0.1$  and  $\alpha_c=0.25$  is employed. Kandlikar [28] prescribes the following equation to compute the Nusselt in the thermally developing region of the domain.

$$Nu_{z,3}(z^+, \alpha_c) = Nu_{z,4}(z^+, \alpha_c) \frac{Nu_{fd,3}(z^+=z_{fd}^+, \alpha_c)}{Nu_{fd,4}(z^+=z_{fd}^+, \alpha_c)} \quad (15)$$

For this analysis, the local Nusselt number and heat transfer coefficient are computed using the heat flux values at various sections. The inside heat transfer coefficient (along the perimeter of the fin) is computed using the following expression.

$$h_i = \frac{q''}{(T_w - T_b)} \quad (16)$$

The wall temperature used in the calculation is found by averaging the temperature across the wall section. The bulk temperature is found by calculating the mass averaged Temperature across the cross section. Nusselt number, may then be computed using the standard relation:

$$h_i = \frac{Nu \cdot k}{D_h} \quad (17)$$

The “inside” heat transfer coefficient is referred to as such in reference to the internal flow through the microchannel. Microchannels, with extremely small characteristic dimensions ( $D_h$ ), thus can exhibit a proportionally larger inside convective heat transfer coefficient.

## 2.6 Thermal Resistance

The thermal resistance to heat transfer for a microchannel heat sink may be expressed as follows (from Chein and Huang [14]):

$$R_{th} = \frac{T_{w,max} - T_{f,in}}{q''} \quad (18)$$

From equation (18),  $q''$  represents the rate of heat rejection from the heat source into the heat transfer liquid through the MCHS.

For this study, the thermal conductivity value for pure silicon was used for all calculations ( $k_s=180$  W/m·K), with constant properties.

## 2.7 Frictional Pressure Loss

The Poiseuille number is defined as

$$Po = fRe \quad (19)$$

Shah and London [30] developed the following correlation for computing the Poiseuille number for fully developed laminar flows in a rectangular channel.

$$fRe = 24(1 - 1.3553\alpha_c + 1.9467\alpha_c^2 - 1.7012\alpha_c^3 + 0.9564\alpha_c^4 - 0.2537\alpha_c^5) \quad (20)$$

Kandlikar [28] developed the following correlations for computing the Poiseuille number in the developing region of the flow for different aspect ratios

$$fRe = \frac{142.1 + 376.69(z^*)^{0.5} + 14010z^*}{1 - 7.3374(z^*)^{0.5} + 800.92z^* - 33.894(z^*)^{1.5}}, \text{ for } \alpha_c = 0.2 \quad (21)$$

$$fRe = \frac{286.65 + 337.81(z^*)^{0.5} + 26415z^*}{1 + 25.701(z^*)^{0.5} + 1091.5z^* + 8.4098(z^*)^{1.5}}, \text{ for } \alpha_c = 0.1 \quad (22)$$

When computing  $fRe$ , the non-dimensional axial coordinate is defined by the following equation.

$$z^* = \frac{z}{D_h} \quad (23)$$

Frictional pressure loss through the MCHS liquid channel is related to the average Fanning friction factor by the following equation:

$$\Delta p = \frac{2f\rho V^2 L}{D_h} \quad (24)$$

The friction factor is also related to the shear stress at the wall by the following relation

$$f = \frac{2 \cdot \tau_w}{\rho V^2} \quad (25)$$

The apparent Poiseuille number is found using the following expression

$$fRe_{app} = \frac{\Delta p D_h^2}{2\mu V L_c} \quad (26)$$

where  $f$  is the Fanning friction factor.

## 2.8 Finite Volume Model

The governing equations for the finite volume model are as described below:

i) For the liquid domain

Conservation of mass/Continuity:  $(\nabla \cdot \bar{V}) = 0$

Conservation of momentum:  $\rho(\nabla \cdot \bar{V})\bar{V} = -\nabla \bar{P} + \mu(\nabla^2 \bar{V}) - \rho(\nabla \cdot \bar{V}'\bar{V}')$

Conservation of energy:  $\rho C_p(\bar{V} \cdot \nabla)\bar{T} = k(\nabla^2 \bar{T}) - \rho C_p(\nabla \cdot \bar{V}'\bar{T}')$

ii) For the solid domain

Energy equation for solid:  $\nabla^2 T = 0$

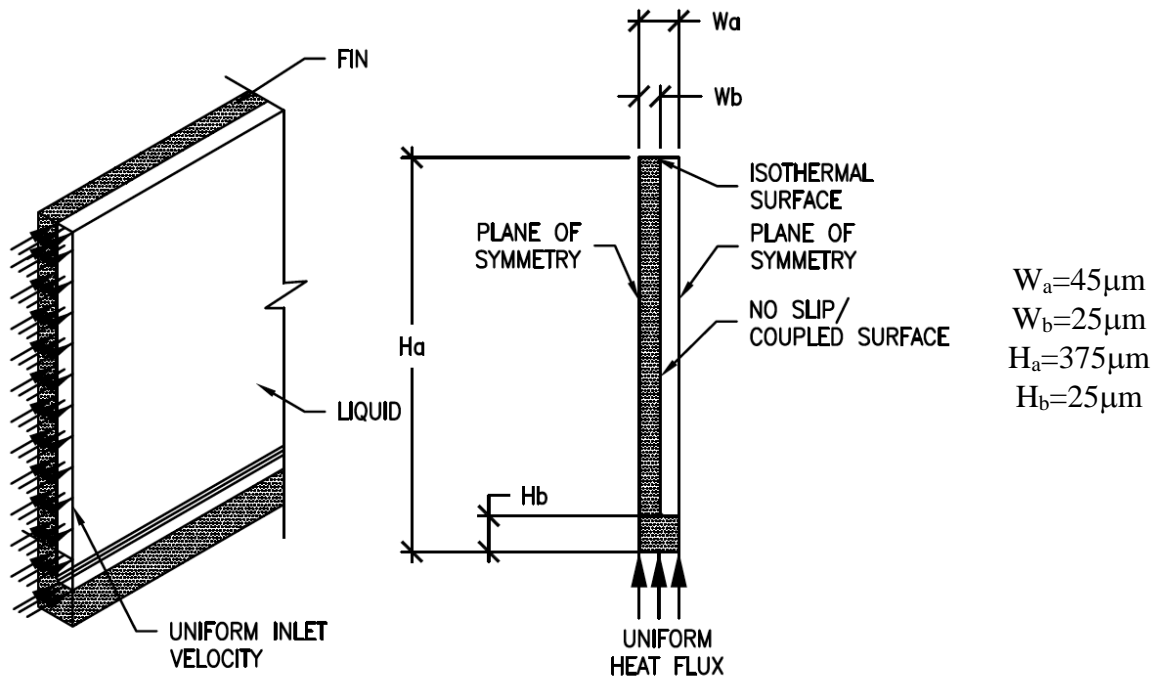


Figure 2. Diagram of solid and liquid domains.

The domain modeled for this study is depicted in Figure 2. The plane of symmetry is assumed to exist since the model enforces laminar flow in the liquid domain. Overall length of the domain is 1 cm. The hydraulic diameter for the fluid domain is 87.8  $\mu\text{m}$ . A uniform heat flux of 1,000,000  $\text{W}/\text{m}^2$  is applied uniformly across the base of the fin section. At the inlet ( $z=0\text{mm}$ ) of the channel, a uniform velocity and temperature is applied. At the outlet ( $z=10\text{mm}$ ) of the channel, the “outlet” condition is applied. At the sides of the domain ( $x=45\mu\text{m}$ ), a symmetry boundary condition is applied. The top of the domain ( $y=375\mu\text{m}$ ) is isothermal. The “no-slip” condition is imposed at the interface between the solid and liquid domains.

This model and mesh were constructed and analyzed using the Ansys Fluent 19.0 simulation package. The mesh is illustrated in Figure 3. The SIMPLE pressure-velocity coupling scheme was employed. The least square cell based gradients, second order pressures, second order upwind momentum and energy spatial discretization were selected for use in the model solution method.



Figure 3. Isometric and front view of model mesh.

### 3. Grid Independence Study

The domain was modeled with several different mesh densities in an effort to determine the density necessary to ensure that the model output approaches a point of stable output.

Table 1. Mesh density study.

Mesh	Total elements	Element size ( $\mu\text{m}$ )	No. of longitudinal divisions	Inlet Pressure (Pa)	Outlet Temp (K)
A	397,100	2.9	190	979,757	318.54
B	418,000	2.9	200	979,312	318.54
C	438,000	2.9	210	979,575	318.54
D	476,800	2.7	200	979,916	318.54
E	333,600	3.2	200	977,838	318.54
F	449,350	2.9	215	979,835	318.54

The boundary conditions are set identically for all meshes and the simulations were run to completion. The fin material is silicon. For model validation runs, the liquid working fluid selected was water. Several key model outputs were then extracted. The data extracted include.

- Mass averaged temperature across the channel outlet plane.
- Area averaged pressure across the channel inlet plan
- Liquid temperature on the z-axis at the base of the channels plane of symmetry
- Liquid temperature and velocity along the y-axis, on the liquid plane of symmetry at the outlet of the channel.
- The results of the study are included in Table 1, and in Figures 4 and 5.

These data indicate that the output for all meshes are qualitatively similar, and have converged to stability. Based on the results of the study, mesh configuration C was selected.

Another series of tests was conducted to determine the critical residual values when solving the system of equations. By observing the residuals change as the solver iterates, it became clear that

the z-velocity equation residual was critical, as it converged the slowest and appeared to have the most significant effect on the results. Three different residual values were examined for their impact on the model output:  $1 \times 10^{-5}$ ,  $1 \times 10^{-6}$  and  $1 \times 10^{-7}$ . Considering this range of residuals the average inlet pressure computed decreased by 0.03% as the residual decreased from  $1 \times 10^{-5}$  to  $1 \times 10^{-6}$ , and only 0.0001% as the residual was decreased from  $1 \times 10^{-6}$  to  $1 \times 10^{-7}$ . Therefore, the residual for the z-velocity equation was set at  $1 \times 10^{-6}$ . Residuals for the continuity equation are in the range of  $1 \times 10^{-4}$ , and decrease somewhat less rapidly than those for the z-velocity. As the z-velocity residuals were changed, the calculated mass flow rate remained essentially unchanged (remaining within 0.0001%). Residuals for the energy equation remained below  $1 \times 10^{-10}$  in all cases, and so were not thought to be a critical variable. The final mesh selected for use in the study is depicted in Figure 3.

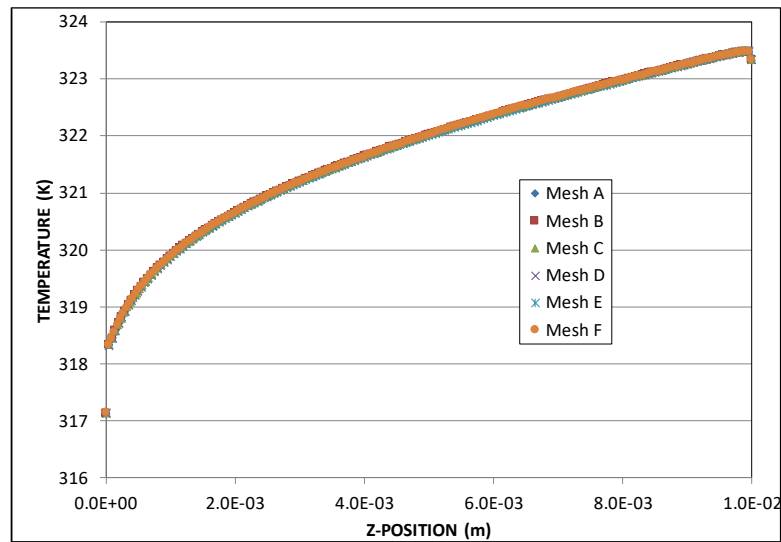


Figure 4. Liquid temperature profile on axis of symmetry at channel surface. ( $x=0$ ,  $y=25\mu\text{m}$ ).

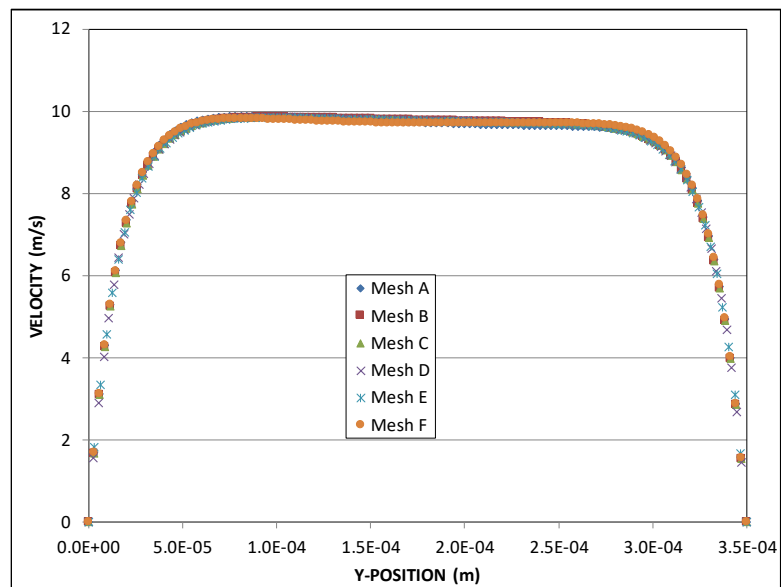


Figure 5. Liquid velocity profile on plane of symmetry,  $x=0$ ,  $z=10\text{mm}$ .

#### 4. Model Validation

In order to validate the model, a simulation using the selected mesh (Mesh C) was executed using the Fluent solver, and relevant model output was compared against an analytical result that is known to be correct. For this model validation, a result from [28] was used as a reference. The channel and the fins modeled for the validation study have the same dimensions as that used for the first part of the validation. The liquid inlet velocity and temperature were set uniformly at 1.245 m/s and 308K, respectively. Kandlikar [28] developed an analytical solution to compute the outlet temperature. Accuracy is tested by comparing the mass-averaged outlet temperature and the area-averaged inlet static pressure computed using the correlations mentioned earlier. In this case, the results generated by the finite volume model agree quite well with the results predicted by the analytical correlations. Using the selected mesh, the computational model predicts that the mass-averaged temperature across the plane of the outlet increases to 317.97K, and the average static pressure at the plane of the inlet is 43.3 kPa. This compares to the analytical solution that predicts a temperature at the outlet of 318K, and inlet static pressure of 43.6 kPa. The difference between the computational solution and the analytical solution in this case is 0.09% and 0.7% respectively.

#### 5. Results

In this study, the performance of several nanofluids in the microchannel described above is examined. The fluids examined include 60% EG, 60%EG/Al<sub>2</sub>O<sub>3</sub>, 60%EG/CuO, and 60%EG/SiO<sub>2</sub>; the volumetric concentration of nanoparticles in the nanofluids varied from 1% to 3%. Several different studies are conducted to isolate the effects of changing various parameters including inlet Reynolds number and inlet average temperature, on the performance of the MCHS.

##### 5.1 Variable Reynolds Number

The first study examines the variation of microchannel performance as the inlet Reynolds number varies from 50 to 300 for 60% EG and the Al<sub>2</sub>O<sub>3</sub>, CuO and SiO<sub>2</sub> nanofluids with concentrations ranging from 1 to 3%. Section properties were extracted from the model using the CFD-Post utility.

Figure 6 illustrates the variation of Nusselt number with non-dimensional length ( $z^+$ ) along the axis of the heat exchanger channel, considering a constant inlet temperature of 308K for the 60% EG and the nanofluids under consideration. The Nusselt number predicted by the correlation referenced in Eq. (15) is superimposed for reference.

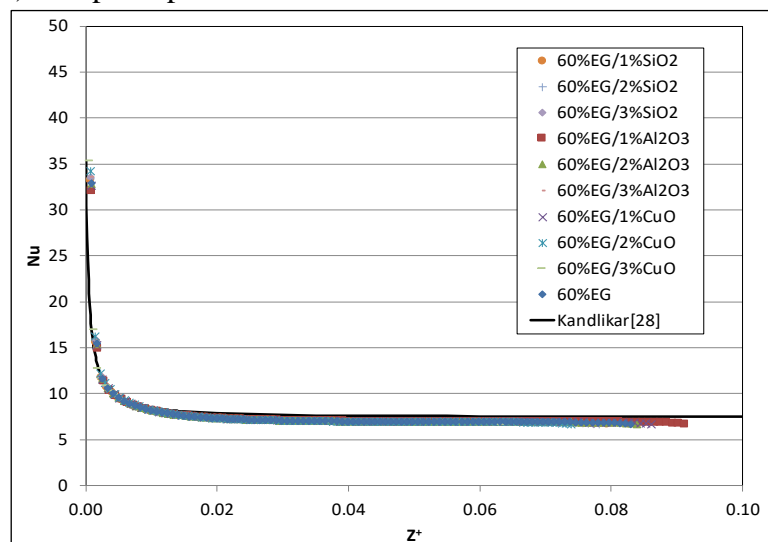


Figure 6. Average Nu versus  $z^+$  for all fluids tested,  $Re=50$ .

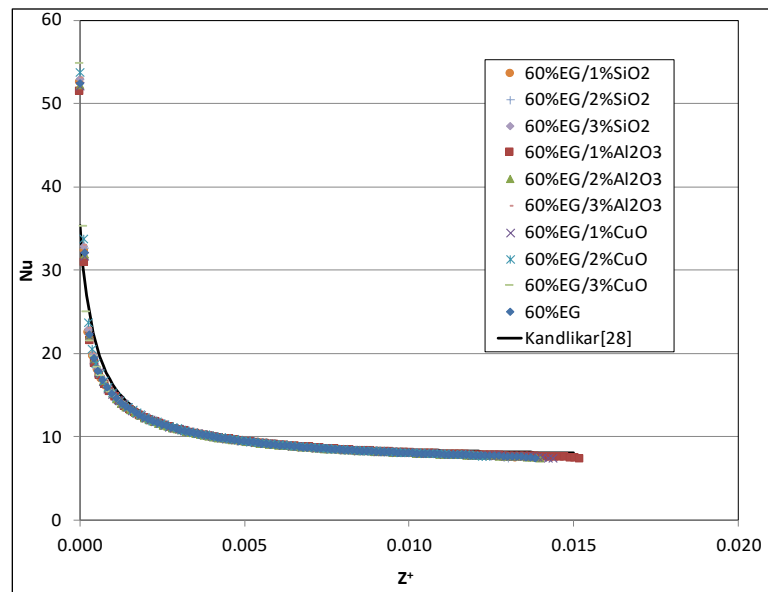


Figure 7. Average Nu versus  $z^+$  for all fluids tested,  $Re=300$ .

At the inlet ( $z=0$ ), the model output for average liquid temperature often did not obey the stipulated boundary condition for inlet temperature, instead generating a value that was typically slightly higher than the stipulated value. This contributed to a singularity in the calculated heat transfer coefficient, as it typically yielded an inverted temperature gradient indicating heat flow out of the liquid stream. In order to improve the quality of the output, therefore, the average value of the liquid at the inlet plane was manually adjusted to match the boundary condition. This made it possible to compute values for heat transfer coefficient and Nusselt number at the inlet plane. The data illustrates that the 60% EG/3% CuO nanofluid has the highest Nusselt number of all the fluids examined, and the base fluid has the lowest Nusselt number at all points along the length of channel.

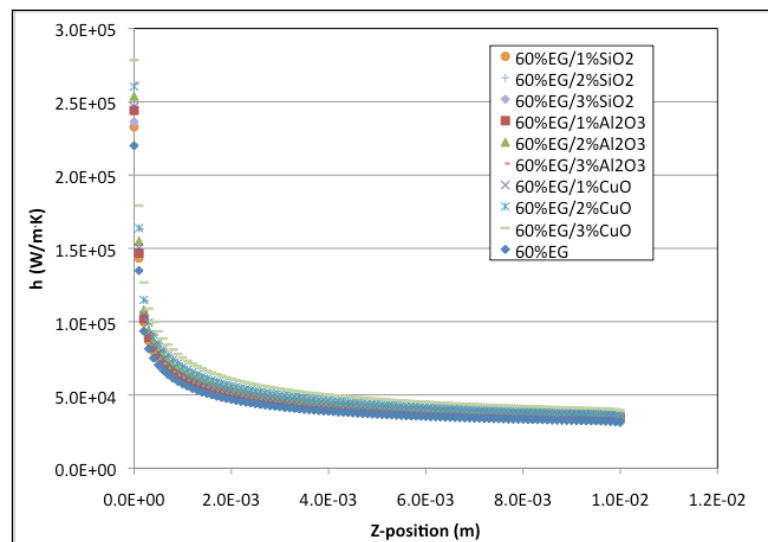


Figure 8. Average heat transfer coefficient versus  $z$ -position for all fluids,  $Re=300$ .

Figure 8 illustrates the variation in average wall heat transfer coefficient for all fluids along the longitudinal axis of the microchannel for  $Re=300$  considering a constant inlet temperature of 308K. This comparison indicates that the 60% EG/3% CuO exhibits the highest heat transfer coefficient of all the fluids tested over the range of Reynolds numbers considered, with an average heat transfer coefficient of  $56,351 \text{ W/m}^2\cdot\text{K}$ . For all Reynolds numbers examined, the heat transfer coefficients generally decrease rapidly near the inlet from an extremely large value, that approaches a steady state value when the flow become thermally fully developed. At the inlet, temperature differentials between the wall and the fluid approach zero, and so the calculated heat transfer coefficient approach infinity.

Figure 9 depicts the average wall heat transfer coefficient along the longitudinal axis of the microchannel as the Reynolds number is varied from  $Re=50$  to  $Re=300$  in increments of 50 for the MCHS with 60%EG/2%  $\text{Al}_2\text{O}_3$  nanofluid. All of the other fluids modeled, including the other nanofluids and the base fluid behave similarly to the 60%EG/2%  $\text{Al}_2\text{O}_3$  nanofluid as Reynolds numbers are increased. At lower Reynolds numbers the heat transfer coefficient for the 60%EG/2%  $\text{Al}_2\text{O}_3$  nanofluid decreases rapidly beyond the inlet to a relatively low value that approaches a steady state value of  $34,450 \text{ W/m}^2\cdot\text{K}$  at  $Z=0.005\text{m}$ ; at higher Reynolds numbers the heat transfer coefficient decreases over the length of the channel, while approaching slightly higher steady state values. For all fluids examined, as the Reynolds number increases, the average value of heat transfer coefficient increases, while the value at the exit changes relatively little.

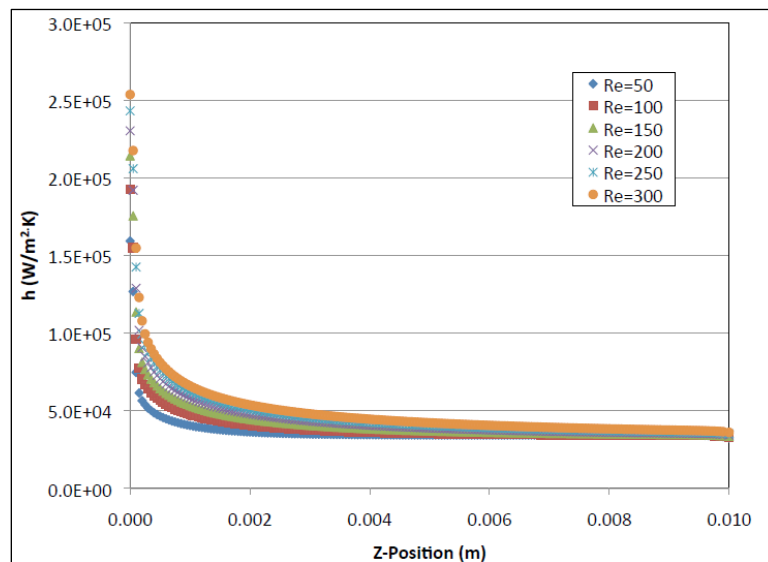


Figure 9. Average heat transfer coefficient versus z-position for 60%EG/2%  $\text{Al}_2\text{O}_3$ .

Figure 10 depicts the average wall heat flux along the z-axis of the domain for  $Re=300$  respectively for all of the fluids examined with constant inlet conditions. The analyses indicate that the heat flux for all fluids examined are very similar over the length of the domain, remaining within 1% from  $Z=0.002\text{m}$  to the outlet. The data for all liquids examined and all Reynolds numbers in the range of 50 to 300 indicate that the heat flux along the longitudinal axis are all very similar despite the large variation in volumetric flow. Since there is constant heat flux at the boundary, this is to be expected.

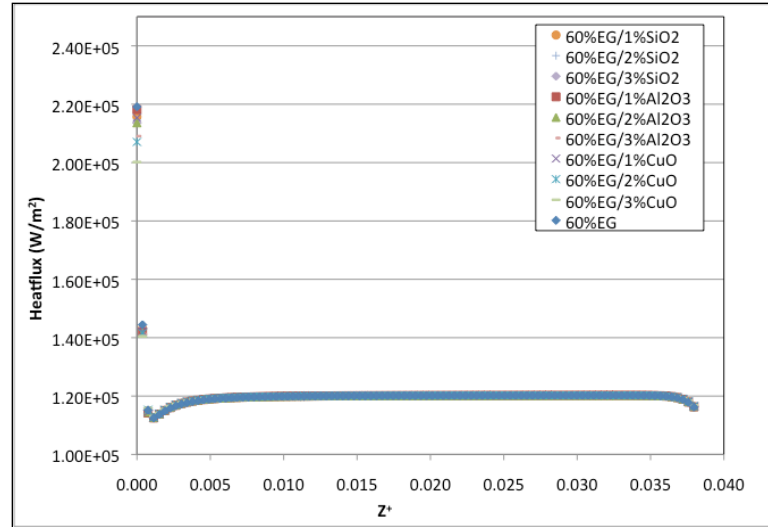


Figure 10. Average wall heat flux versus  $z^+$  for all fluids,  $Re=300$ .

Average values for the wall heat transfer coefficient ( $h$ ), and Nusselt number for 60%EG/2%  $Al_2O_3$ , from  $Re=50$  to  $Re=300$  are reported in Table 2.

Table 2. Average values for  $h$  and  $Nu$  for 60%EG/2%  $Al_2O_3$ .

<b>Re</b>	<b><math>h_{avg}(W/m^2 \cdot K)</math></b>	<b><math>Nu_{avg}</math></b>
50	37,331.31	7.56
100	40,000.73	8.16
150	42,695.44	8.74
200	45,240.06	9.27
250	47,608.10	9.76
300	50,202.41	10.22

The values for average Nusselt number reported in this study tend to deviate significantly from those reported by others for rectangular microchannels considering traditional T (constant temperature), H1 (axially constant wall heat flux and circumferentially constant temperature), and H2 (uniform wall heat flux) boundary conditions. The average Nusselt numbers found for the modeled fluids are considerably higher than those reported by [28] for an aspect ratio of 0.143. The values are 6.1, 5.4, and 3 for T, H1 and H2 boundary conditions, respectively. This reflects the impact of the various deviations from the assumptions implicit in those classic boundary conditions.

Tables 3 and 4 contain tabular performance data for the MCHS with nanofluids and the base fluid at Reynolds numbers 50 and 300. These tables illustrate the impact of the fluids' different properties on the performance of the MCHS. For  $Re=50$ , the 60%EG/3% CuO produces the lowest average base temperature, and has the highest average inside heat transfer coefficient. In contrast, it exhibits the highest required pressure at the inlet as well as required hydraulic pumping power. At  $Re=300$ , the MCHS with 60%EG/3% CuO again yields the lowest average base temperature, and the highest average inside heat transfer coefficient. However, it has the highest inlet pressure requirement and hydraulic power. The pressure requirement at the inlet of the channel considering the 60% EG at an inlet  $Re=300$  is 1,608 kPa, while for the 60% EG/3% CuO is 4,703 kPa, a difference of 192%. The difference in the hydraulic power required to drive the flow of 60%EG/3%

CuO at  $Re=300$  reflects the greater volumetric flow compared to the 60%EG. It is 366% higher for the nanofluid than that required for the base fluid. At  $Re=300$ , the microchannel with 60% EG/3% CuO nanofluid has an average base temperature that is 1K lower than that for the microchannel with 60% EG. Due to the large difference in viscosity and fluid density between the 60% EG and the 60% EG/3% CuO, this represents a significant difference in mass flow, with required mass flow rates for the channel of  $1.885 \times 10^{-4} \text{ kg/s}$  and  $3.441 \times 10^{-4} \text{ kg/s}$  for 60% EG and 60% EG/3% CuO nanofluids, respectively (the mass flow rate for the 60% EG/3% CuO is 83% higher than for the base fluid in this case).

Table 3. Average values, all fluids with constant inlet Reynolds number ( $Re=50$ ).

Fluid	$T_{avg}$ (K)	$h_{avg}$ (W/m <sup>2</sup> K)	$P_{avg}$ (Pa)	$\dot{W}$ (mW)
60% EG	318.036	31,987.00	234,147	6.84
60%EG/1% CuO	317.193	36,572.28	299,613	9.64
60%EG/2% CuO	316.351	37,869.97	463,471	17.91
60%EG/3% CuO	315.63	40,143.19	708,979	32.97
60%EG/1% SiO	317.468	33,970.40	310,312	10.27
60%EG/2% SiO	317.361	34,054.12	346,122	12.12
60%EG/3% SiO	317.253	34,199.40	388,167	14.34
60%EG/1% Al <sub>2</sub> O <sub>3</sub>	317.45	36,531.84	288,438	9.18
60%EG/2% Al <sub>2</sub> O <sub>3</sub>	316.917	37,331.31	369,129	13.04
60%EG/3% Al <sub>2</sub> O <sub>3</sub>	316.448	38,449.24	460,964	18.10

Table 4. Average values, all fluids with constant inlet Reynolds number ( $Re=300$ ).

Fluid	$T_{avg}$ (K)	$h_{avg}$ (W/m <sup>2</sup> K)	$P_{avg}$ (Pa)	$\dot{W}$ (mW)
60% EG	313.404	43,187.17	1,608,600	281.77
60%EG/1% CuO	312.99	48,730.59	2,040,540	393.77
60%EG/2% CuO	312.689	52,068.71	3,112,490	721.75
60%EG/3% CuO	312.392	56,351.44	4,702,510	1,312.27
60%EG/1% SiO	313.157	45,865.74	2,121,080	421.26
60%EG/2% SiO	313.119	46,215.44	2,364,530	496.78
60%EG/3% SiO	313.078	46,623.21	2,633,800	584.02
60%EG/1% Al <sub>2</sub> O <sub>3</sub>	313.075	48,061.04	1,969,940	376.33
60%EG/2% Al <sub>2</sub> O <sub>3</sub>	312.879	50,202.41	2,499,740	530.14
60%EG/3% Al <sub>2</sub> O <sub>3</sub>	312.705	52,233.60	3,101,160	730.60

Figure 11 graphically depicts the liquid temperatures on the plane of symmetry along the center axis ( $x=0$ ) of the domain for the 60% EG/2% Al<sub>2</sub>O. This graphic illustrates that for Reynolds number greater than 100, the flow does not achieve full thermal development, as the temperature of the center plane remains at 308K for nearly the entire length of the channel. For  $Re=50$ , the graphic indicates the thermal effect at the wall penetrates the symmetry plane at approximately  $z=0.3$  cm. At  $Re=100$ , the thermal wall effects penetrate the symmetry plane at approximately  $z=0.7$  cm. This illustrates that there is a point of diminishing returns for lowering the base temperature as flows through the MCHS are increased, the thermal effects of the wall do not reach the axis of symmetry for Reynolds number slightly greater than 150.

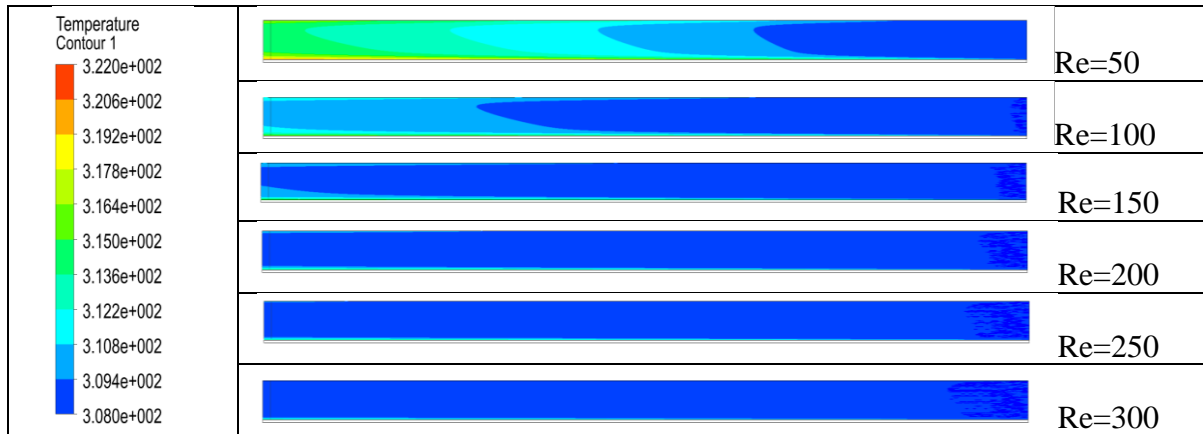


Figure 11. Longitudinal axis liquid temperature, 60%EG/2%  $\text{Al}_2\text{O}_3$ .

In Figure 12, the R-value of all fluids tested is plotted with respect to inlet Reynolds number. The data indicates that the lowest R-values are generated by the 60%EG/3% CuO nanofluid. The highest R-values are generated for the 60% EG. All of the nanofluids studied exhibited lower R-values than the base fluid over the range of Reynolds numbers evaluated, with the 60%EG/3% CuO exhibiting the lowest R-value.

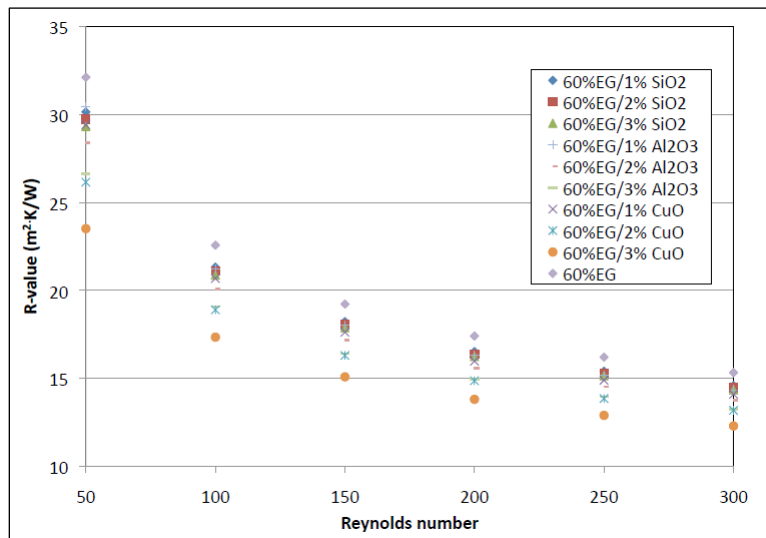


Figure 12. Average R-value for all fluids.

Figure 13 is a plot of the average temperature of the microchannel considering the same range of variables. In this case, the 60%EG/3% CuO also exhibits the lowest base temperature of all fluids examined for all Reynolds numbers studied. The 60% EG, in contrast, exhibited the highest average base temperatures of all. At  $\text{Re}=50$  the average base temperature for the 60%EG/3% CuO filled microchannel is 2.4K lower than that of the microchannel filled with 60%EG. The difference in average base temperatures between the 60%EG and the 60%EG/3% CuO decreases with increasing Reynolds number. At  $\text{Re}=300$ , the difference between the average base temperature for the base fluid and the nanofluid decreases to 1K. All of the nanofluids studied are predicted to decrease the average base temperature relative to that for the base fluid at equal Reynolds number. This is an important finding, as maintaining lower base substrate temperatures presumably

increases the reliability of integrated circuit systems due to the reduction in thermal stresses across the domain.

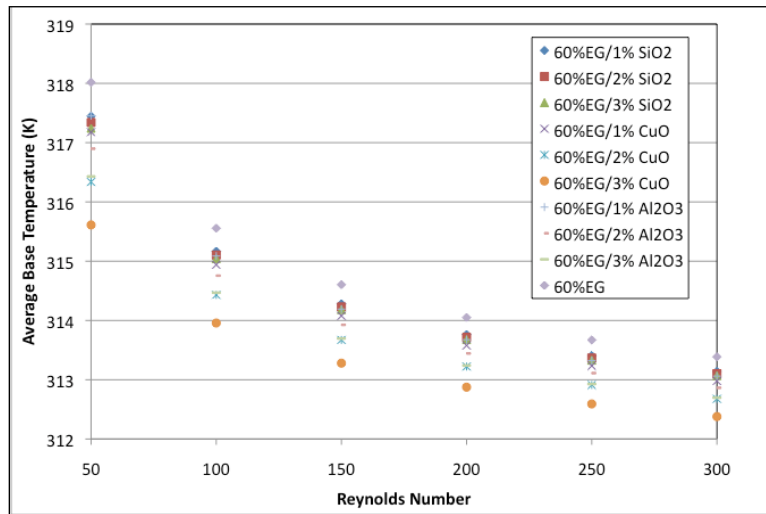


Figure 13. Average base temperature for all fluids.

In Figures 14 and 15, contain graphs of the Poiseuille number for all liquids examined over the length of the microchannel for Reynolds numbers 50 and 300, respectively. The values predicted by [28] are superimposed for reference. The Poiseuille numbers are nearly equal over the length of the domain for all the liquids examined. Using Eq. (12), the hydraulic entrance length for the flows examined here range from 0.022 cm to 0.13 cm in length as Reynolds number increases from 50 to 300. The modeling data indicates that the Poiseuille number approaches a steady state value at  $z=0.05$  cm and  $z=0.25$  cm at Reynolds number 50 and 300, respectively.

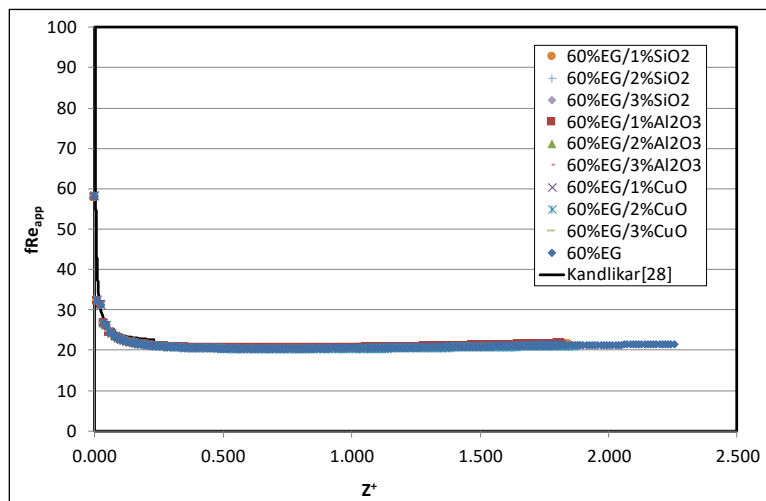


Figure 14. Poiseuille number variation with axial position,  $Re=50$ .

At  $Re=50$ , the Poiseuille number for the fluids drop steeply at the inlet, to a fully developed value of 22.3-22.7, depending on the liquid, at  $z^*=0.0251$ . At  $Re=300$ , the Poiseuille decreases rapidly from the inlet to a fully developed value 23.1 at  $z^*=0.014$ . These modeled values compare to values for Poiseuille number of 27.9 and 35.0 as predicted by [28], at the Reynolds numbers of 50 and 300.

In this case, the model predicts that the friction factor for the flow is lower than that predicted by the previously published correlation.

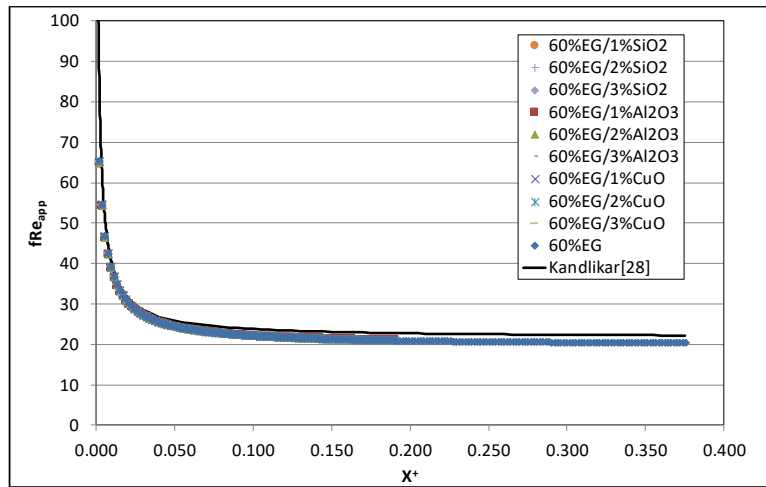


Figure 15. Poiseuille number variation with axial position,  $Re=300$ .

## 5.2 Constant Inlet Velocity

Table 5 contains calculated average values for average base temperature, inside heat transfer coefficient and inlet pressure for all of the fluids examined, with inlet temperature held at 308K and inlet velocity held constant at 5 m/s.

Table 5. Average values, all fluids with constant inlet velocity (5 m/s).

Fluid	Re	$T_{avg}$ (K)	$h_{avg}$ (W/m <sup>2</sup> K)	$P_{avg}$ (Pa)
60% EG	157.75	314.625	36,902.21	771,020
60%EG/1% CuO	142.49	314.282	40,769.45	884,285
60%EG/2% CuO	119.62	314.194	41,603.69	1,115,225
60%EG/3% CuO	98.73	314.091	43,150.99	1,392,176
60%EG/1% SiO	135.86	314.554	38,269.96	890,864
60%EG/2% SiO	130.44	314.617	38,101.43	935,384
60%EG/3% SiO	125.18	314.672	38,004.48	985,649
60%EG/1% Al <sub>2</sub> O <sub>3</sub>	142.94	314.382	40,505.53	862,897
60%EG/2% Al <sub>2</sub> O <sub>3</sub>	128.69	314.311	41,302.50	982,264
60%EG/3% Al <sub>2</sub> O <sub>3</sub>	118.49	314.26	41,894.76	1,091,836

The 60% EG/3% CuO nanofluid generated the lowest modeled average base temperature, and the highest average heat transfer coefficient over the length of the fin. The microchannel modeled with 60% EG generated the lowest required pressure at the inlet for the specified average inlet velocity. Considering constant inlet velocity (as illustrated in Table 5), the average base temperature for the 60% EG/3% CuO is 0.53K lower than that for the 60% EG. In this case, the required pressure at the inlet is 80% higher than that for the base fluid. In this case, the hydraulic power required is directly proportional to the pressure at the inlet, since volumetric flows are equal considering equal entering velocity.

### 5.3 Variable Inlet Temperature

Experiments have shown that the thermophysical properties of various nanofluids change significantly with temperature. In particular, thermal conductivity and specific heat increase mildly with increasing temperature, while density decreases mildly with increasing temperature. In contrast, viscosity decreases strongly with increasing temperature (the viscosity of both 60% EG and 60%EG/2%  $\text{Al}_2\text{O}_3$  both decrease by approximately 25% as bulk temperature increases from 306K to 316K). This has the potential to impact heat transfer performance.

To quantify the effect of changing liquid inlet temperature on the heat transfer performance of the MCHS, a series of runs with 60%EG/2%  $\text{Al}_2\text{O}_3$  with inlet set at  $\text{Re}=150$ , and varying inlet temperature from 306K to 316K were performed. In Figure 16, the variation of Nusselt number with changing inlet liquid temperature is presented graphically. This shows that the Nusselt numbers are slightly higher for lower inlet liquid temperatures near the inlet. The curves once again approach a value of 7 with increasing  $Z$ .

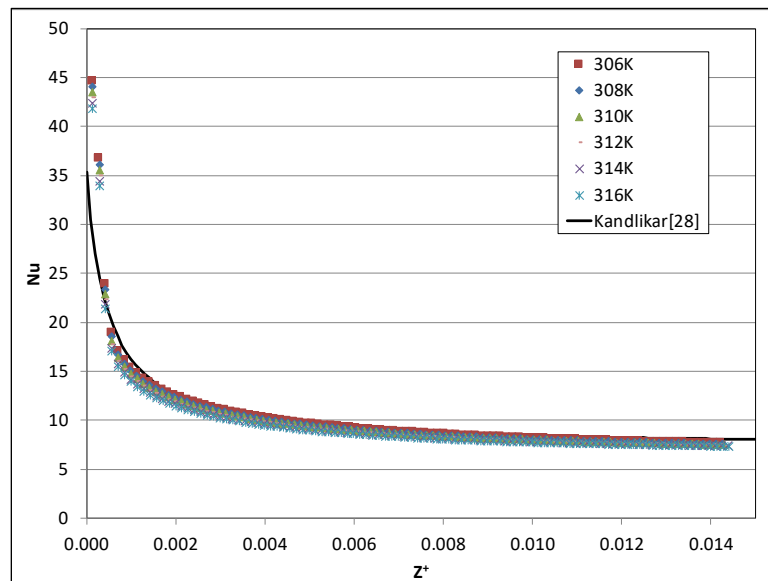


Figure 16. Nusselt number variation with  $Z$ -position, considering multiple temperatures for 60%EG/2%  $\text{Al}_2\text{O}_3$   $\text{Re}=150$ .

The average wall heat transfer coefficient for all inlet temperatures considered are depicted in graphic form in Figure 17. These plots all end up nearly coincident, despite the change in viscosity expected over the 10K temperature range. The average heat transfer coefficient for 60% EG/2%  $\text{Al}_2\text{O}_3$  nanofluid ranges from 42,841  $\text{W}/\text{m}^2\text{K}$  at 306K to 42,345  $\text{W}/\text{m}^2\text{K}$  at 316K, a decrease of 1.1%.

In Figure 18, the calculated friction factor between inlet temperature 306K and 316K is illustrated. For this metric, calculated values remain nearly constant as the inlet temperature increases through the range.

## 6. Conclusions

A nanofluid filled MCHS was simulated using conjugate heat transfer and fluid dynamic, three-dimensional finite volume modeler assuming a fixed heat flux through the base. The analysis show that the model generates Nusselt and Poiseuille numbers that agree qualitatively with the existing

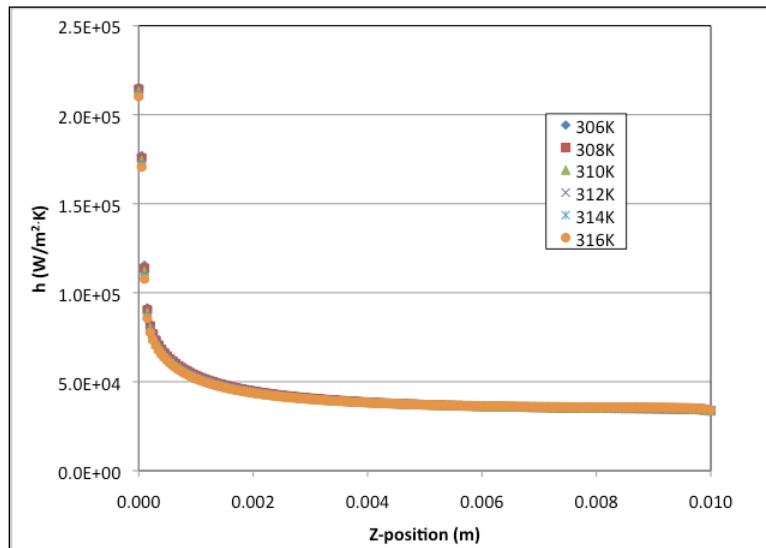


Figure 17. Heat transfer coefficient variation with Z-position, for 60%EG/2%  $\text{Al}_2\text{O}_3$  at multiple inlet temperatures.

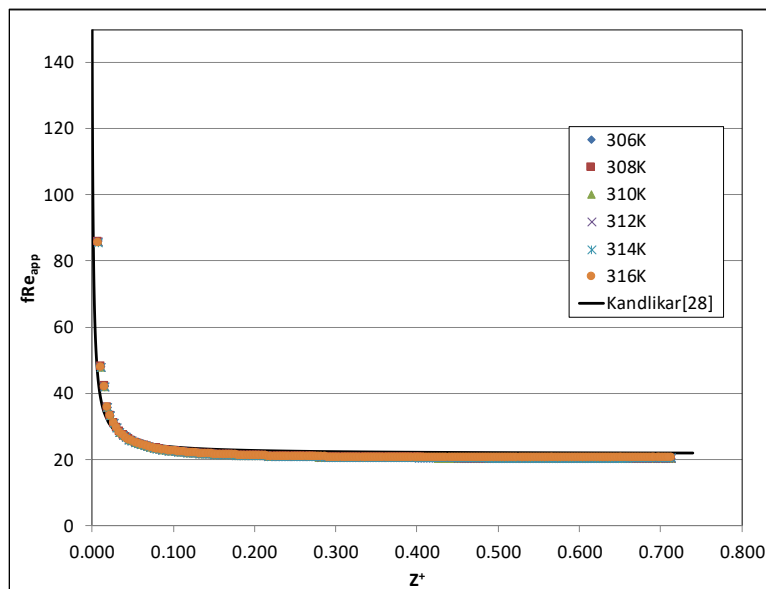


Figure 18. Poiseuille number variation with axial position, for 60%EG/2%  $\text{Al}_2\text{O}_3$   $\text{Re}=150$  considering multiple inlet temperatures.

correlations proposed by Kandlikar [28]. The significant findings based on a detailed examination of the model data are summarized thusly:

- Of the nanofluids studied, the 3% CuO/60% EG exhibits the biggest improvement in the average heat transfer coefficient compared to the base fluid over the range  $50 \leq \text{Re} \leq 300$ . The average inside heat transfer coefficient for the 3% CuO/60% EG nanofluid exceeds that of the base fluid by 30% at  $\text{Re}=300$ . The average heat transfer coefficient for the 3% CuO/60% EG is 25% higher than that for 60% EG at  $\text{Re}=50$ , and 17% higher when compared at a constant inlet velocity of 5 m/s.

- Similarly, the thermal resistance of the MCHS with 3% CuO/60% EG was 24% lower than that for the base fluid at  $Re=50$  and 19% lower at  $Re=300$ . All of the nanofluids lowered the overall thermal resistance of the system when compared on a constant Reynolds number basis.
- Considering equal inlet Reynolds number, all of the nanofluids examined lowered the average temperature on the base of the solid domain. At best, the base temperature reduction predicted in the model is 2.4K. In applications where MCHS are used with nanofluids for component cooling, lower operating temperatures may contribute to increased component life and system reliability.

As expected, the improvement in heat transfer performance of an MCHS with nanofluids comes at the cost of higher frictional pressure losses and pumping power. At  $Re=300$ , the 60% EG/3% CuO generates frictional pressure losses 192% higher than those for the base fluid. Pumping power for the nanofluid exceeds that for the base fluid by 366%. The increase in power requirements and energy consumption associated with pumping more viscous nanofluids versus their respective base fluids must be balanced against absolute improvements in the system thermal performance.

## References

- [1] B. C. Pak, and Y. I. Cho, Hydrodynamic and Heat Transfer Study of Dispersed Fluids With Submicron Metallic Oxide Particles, *Experimental Heat Transfer* vol 11, pp. 151-170, 1998.
- [2] R. Vajjha, Measurement of Thermophysical Properties of Nanofluids and Computation of Heat Transfer Characteristics, M. S. Thesis, University of Alaska Fairbanks, pp.150, 2008.
- [3] C. H. Chon, K. Kihm, S. Lee and S. U. S. Choi, Empirical Correlation Finding the Role of Temperature and Particle Size for Nanofluid ( $Al_2O_3$ ) Thermal Conductivity Enhancement, *Applied Physics Letters*, vol 87, pp. 153107-1 - 153107-3, 2005.
- [4] S. P. Jang and S. U. S. Choi, Effects of Various Parameters on Nanofluid Thermal Conductivity, *Journal of Heat Transfer*, vol 129, pp. 617-623, 2007.
- [5] R. Vajjha, and D. K. Das, Experimental Determination of Thermal Conductivity of Three Nanofluids and Development of New Correlations, *International Journal of Heat and Mass Transfer*, vol 52, pp. 4675-4682, 2009.
- [6] J. Koo and C. Kleinstreuer, A New Thermal Conductivity Model for Nanofluids, *Journal of Nanoparticle Research*, vol 6, pp. 577-588, 2004.
- [7] P. K. Namburu, D. P. Kulkarni, D. Misra and D. K. Das, Viscosity of Copper Oxide Nanoparticles Dispersed in Ethylene Glycol and Water Mixture, *Experimental Thermal and Fluid Science*, vol 32, pp. 397-402, 2007.
- [8] R. Vajjha and D. K. Das, Specific Heat Measurement of Three Nanofluids and Development of New Correlations, *Journal of Heat Transfer*, ASME, New York, vol 131, pp. 7, 2009.
- [9] D. Faulkner, M. Khotan and R. Shekhariz, Practical Design of a  $1000\text{ W/m}^2$ , *Proceedings IEEE Semiconductor Thermal Measurement and Management Symposium*, pp. 223-230, 2003.
- [10] C. J Ho, L. C. Wei and Z. W. Li, An experimental investigation of forced convective cooling performance of a microchannel heat sink with  $Al_2O_3$ /water nanofluid, *Applied Thermal Engineering*, vol 30, pp. 96-103, 2010.

- [11] J. Lee and I. Mudawar, Assessment of the effectiveness of nanofluids for single-phase and two-phase heat transfer in micro-channels, *International Journal of Heat and Mass Transfer*, vol 50, pp. 452-463, 2007.
- [12] X. F. Peng, G. P. Peterson and B. X. Wang, Heat transfer characteristics of water flowing through microchannels, *Experimental Heat Transfer*, vol 7, pp. 265-283, 1994.
- [13] J. Jung, H. Oh and H. Kwak, Forced convective heat transfer of nanofluids in microchannels, *International Journal of Heat and Mass Transfer*, vol 52, pp. 466-472, 2009.
- [14] R. Chein and G. Huang, Analysis of Microchannel Heat Sink Performance Using Nanofluids, *Applied Thermal Engineering*, vol 25, pp. 3104-3114, 2004.
- [15] J. Koo and C. Kleinstreuer, Laminar Nanofluid Flow in Microheat-Sinks, *International Journal of Heat and Mass Transfer*, vol 48(13), pp. 2652-2661.
- [16] S. P. Jang and S. U. S. Choi, Cooling Performance of a Microchannel Heat Sink with Nanofluids, *Applied Thermal Engineering*, vol 26, pp. 2457-2463, 2006.
- [17] D. Leela, The performance evaluation of  $Al_2O_3$ /water nanofluid flow and heat transfer in microchannel heat sink, *International Journal of Heat and Mass Transfer*, vol 54, pp. 3891-3899, 2011.
- [18] A. Bar-Cohen, Ed., *Encyclopedia of Thermal Packaging, Set 3: Thermal Packaging Applications*, World Scientific Publishing Co. Inc., New Jersey, 2018, [www.worldscientific.com](http://www.worldscientific.com).
- [19] J. R. Thome, Ed., *Encyclopedia of Two-Phase Heat Transfer and Flow IV: Modeling Methodologies, Boiling of CO<sub>2</sub>, and Micro-Two-Phase Cooling*, World Scientific Publishing Co. Inc., New Jersey, 2018, [www.worldscientific.com](http://www.worldscientific.com).
- [20] L. Snoussi, N. Ouerfelli, K. V. Sharma, N. Vrinceanu, A. J. Chamkha and A. Guizani, Numerical Simulation of Nanofluids for Improved Cooling Efficiency in a 3D Copper Microchannel Heat Sink (MCHS), *Physics and Chemistry of Liquids*, pp. 1-21, 2017.
- [21] ASHRAE Handbook, Fundamentals, American Society of Heating, Refrigeration and Air-Conditioning Engineers, Inc., Atlanta, GA, Ch. 21, 2005.
- [22] J. Buongiorno, Convective Transport in Nanofluids, *Journal of Heat Transfer*, vol 128, pp. 240-250, 2006.
- [23] R. S. Vajjha, D. K. Das and D. P. Kulkarni, Development of new correlations for convective heat transfer and friction factor in turbulent regime for nanofluids, *International Journal of Heat and Mass Transfer*, vol 53(21-22), pp. 4607-4618, 2010.
- [24] F. M. White, *Viscous Fluid Flow*, 2nd Ed., McGraw Hill, New York, 1991.
- [25] D. Ray, et al., Experimental and Numerical Investigations of Nanofluids Performance in a Compact Minichannel Plate Heat Exchanger, *International Journal of Heat and Mass Transfer*, vol 71, pp. 732-736, 2014.
- [26] B. C. Sahoo, D. K. Das, R. S. Vajjha and J. R. Satti, Measurement of the thermal conductivity of silicon dioxide nanofluid and development of correlations, *Journal of Nanotechnology in Engineering and Medicine*, vol 3(4), pp. 041006-041006, 2013.
- [27] R. L. Hamilton and O. K. Crosser, Thermal Conductivity of Heterogeneous Two-Component Systems," *Industrial and Chemical Engineering* vol 1, pp. 187-191, 1962.
- [28] S. Kandlikar, S. Garimella, D. Li, S. Colin and M. R. King, *Heat Transfer and Fluid Flow in Minichannels and Microchannels*, Elsevier, Amsterdam, pp. 87-136.

- [29] L. S. Han, Hydrodynamic Entrance Lengths for Incompressible Laminar Flow in Rectangular Ducts, *Journal of Applied Mechanics*, vol 27, pp. 403-409, 1960.
- [30] R. K. Shah and A. L. London, *Laminar Forced Flow Convection in Ducts*, Supplement 1 to *Advances in Heat Transfer*, New York: Academic Press, 1978.
- [31] R. C. Reid, J. M. Prausnitz and T. K. Sherwood, *The Properties of Gases and Liquids*, 4<sup>th</sup> ed., McGraw Hill, New York, 1987.